Wavelet leaders and bootstrap for multifractal analysis of images

Herwig Wendt [a], Stéphane G. Roux [a], Stéphane Jaffard [b,*], Patrice Abry [a]

[a] *CNRS and Ecole Normale Supérieure de Lyon, France*
[b] *CNRS and Université Paris Est, France*

ARTICLE INFO

ABSTRACT

Multifractal analysis is considered a promising tool for image processing, notably for texture characterization. However, practical operational estimation procedures based on a theoretically well established multifractal analysis are still lacking for image (as opposed to signal) processing. Here, a wavelet leader based multifractal analysis, known to be theoretically strongly grounded, is described and assessed for 2D functions (images). By means of Monte Carlo simulations conducted over both self-similar and multiplicative cascade synthetic images, it is shown here to benefit from much better practical estimation performances than those obtained from a 2D discrete wavelet transform coefficient analysis. Furthermore, this is complemented by the original analysis and design of procedures aiming at practically assessing and handling the theoretical function space embedding requirements faced by multifractal analysis. In addition, a bootstrap based statistical approach developed in the wavelet domain is proposed and shown to enable the practical computation of accurate confidence intervals for multifractal attributes from a given image. It is based on an original joint time and scale block non-parametric bootstrap scheme. Performances are assessed by Monte Carlo simulations. Finally, the use and relevance of the proposed wavelet leader and bootstrap based tools are illustrated at work on real-world images.

1. Introduction: multifractal analysis for image processing

Nowadays, in a large number of applications of very different natures, the *data* collected by sensors for analysis consist of *images*, i.e., they are naturally bi-dimensional *signals*. This is mostly due to the recent and significant progresses achieved in digital sensor, fast rate and high resolution camera and video camera design. For a number of these applications the corresponding statistical analysis of the images amounts to performing texture character-ization. This is the case notably for clouds or rainfalls analyses in geophysics [1–3], bio-medical diagnosis for human body rhythms or structure (bones, tissues, mam-mography, etc.) [4–6], universe or galaxy structures in astronomy [7], growth phenomena in physics [8,9] or texture classification in computer vision [10,11], to name but a few examples.

Texture characterization is now often envisaged by measuring the fluctuations (with respect to space) of the regularity of the amplitude of the image. There is an increasing number of research articles suggesting that regularity characterization should be conducted within the mathematical framework of multifractal analysis (MA). In practice, MA is quasi-systematically performed using the coefficients of continuous [12] or discrete [13,14] wavelet transforms. The regularity fluctuations are then inferred from the behavior in the limit of fine scales of the (sample mean estimators of the) moments of order q. However, surveying the literature related to applications, one realizes that image MA suffers from two major limi-tations: It remains either incomplete, as it is simplified to the computation of Fourier spectra (via classical standard spectral estimation) or of wavelet coefficients variograms (regression of the variance against the scales), i.e., for both

* Corresponding author.
  E-mail addresses: herwig.wendt@ens-lyon.fr (H. Wendt), stephaneg.roux@ens-lyon.fr (S.G. Roux), jaffard@univ-paris12.fr (S. Jaffard), patrice.abry@ens-lyon.fr (P. Abry).

cases, of a second order statistical quantity only (e.g., [15]); or it is reduced to the analyses of collections of 1D slices of data instead of real 2D images (e.g., [16]).

The reasons for this are mostly associated to the theoretical requirement that a complete MA involves, namely a variety of negative statistical orders q as well as positive ones [17,18]. However, wavelet coefficients, by nature, consist of quantities that mostly concentrate around 0, rendering the numerical computation of negative q moments extremely unstable or even theoretically infinite. To overcome this limitation, using the modulus maxima of a continuous wavelet transform (MMWT) has been proposed for the 1D case [12]. This method relies on the determination of the coefficients of a continuous wavelet transform (CWT), from which a skeleton, consisting of maxima along scales lines, is extracted [19]. The wavelet coefficients living on this skeleton are then involved in the computation of the fluctuations of the image regularity. For details, the reader is referred to [12]. This technique has been further extended to image analysis, at the price though of significant computational (2D-CWT + 2D-Skeleton) and conceptual complexities (maxima lines become maxima manifolds) [20]. Therefore, it remains hardly ever used for images (see, a contrario, [20]). In addition to the practical difficulties related to its implementation, the MMWT approach, be it 1D or 2D, despite its showing satisfactory experimental performances, is still lacking a theoretical mathematical support.

Recently, an alternative approach has been proposed [14,17]: the wavelet leader (WL) MA. This method is theoretically backed up by a strong mathematical framework [14,17,21,26]. Also, its being defined from an (orthonormal) discrete wavelet transform (DWT) enables reasonably easily its theoretical and practical extensions to higher dimension [14,21]. It has been shown to be one of the best available tools for (1D) signals, enabling a relevant and general MA of empirical data, with both excellent theoretical properties and statistical performance [22].

Therefore, elaborating on theoretical results proven for functions in $\mathbb{R}^n$ and recently published in [14,17,21,26], the *first goal* of the present contribution is to provide practitioners with an explicit formulation of a 2D WL based MA that can actually be applied to real-world images. To this end, Section 2 reviews the key notions underlying MA, introduces the 2D WL MA, and details the corresponding practical estimation procedures. In addition, the validity and practical relevance of these 2D MA procedures are assessed in the present work by numerical simulation studies of their estimation performance in Sections 6.1 and 6.2. The performances of the proposed procedures is shown to compare very favorably to those obtained from wavelet coefficients. The synthetic self-similar and multiplicative cascade images used in Monte Carlo simulations are described in Section 5.

The *second goal* of the present contribution is to further complement the theoretical understanding of a comprehensive use of the WL MA. For this, we address a number of theoretical issues, related to which function space data are embedded in, and constituting mandatory prerequi-

sites in the derivation of the WL based MA, as well as for any other procedure aiming at performing a MA of images or signals. Notably, the WL MA is well-defined for bounded functions only. However, a digital image consisting of an intensity local average can naturally be seen as the approximation—at a given resolution level—of a positive measure, and there is hence no a priori guarantee for it to belong to the space of bounded functions. Section 3 addresses such issues and proposes tools for an a priori analysis aiming at enabling the characterization of which function space the data belong to, and solutions to handle the bounded function requirement. This part has practical implications for the validation of many image processing models, where an a priori assumption is made on the function spaces that contain the image. The proposed solutions are supported by mathematical proofs, whose founding arguments are reported in Section 3 (yet in Section 3.3 detailed versions of some proofs are beyond the scope of the present article and will be published independently in a theoretically oriented journal, see [34]). The performances of the proposed procedures is assessed numerically. Also, their practical relevance and usefulness are supported through the examination of the large reference texture image database used in [11].

In the use of MA in actual applications, practitioners are potentially as much interested in the confidence that should be granted to the estimates as in the value of the estimates themselves. However, the (asymptotic) statistical performances of the estimation procedures for multifractal attributes—and hence the design of confidence intervals are beyond analytic derivation, mostly because of the involved statistical properties of multifractal images. To overcome such limitations, we recently proposed, for 1D signal, the use of non-parametric bootstrap techniques [23,24], applied in the wavelet domain [22,25]. Therefore, the *third goal* of the present contribution is to define an original bootstrap scheme that matches the 2D WL MA and to validate its performances in producing confidence intervals for multifractal attributes from a single image. This 2D scheme differs from the 1D one proposed earlier insofar as it consists of a joint time and scale block bootstrap procedure, designed to better account for the naturally joint time and scale correlation structure of wavelet coefficients and WLs. This bootstrap approach is detailed in Section 4. The statistical performances of this bootstrap scheme, its relevance and usefulness are assessed numerically and discussed in Section 6.3.

The relevance and practical use of the multifractal leader and bootstrap based analysis framework proposed here is illustrated at work on a real-world image (cf. Section 6.4). Also, comments and discussions related to the general applicability to images conditions of the proposed leader and bootstrap based MA procedures are proposed in Section 6.5.

2. Multifractal formalism and wavelet leader

This section aims at providing to practitioners in image processing actual procedures to conduct relevant MA of

real-world images. It is based on general theoretical results published in [14,17,21,26] and makes explicit their formulation and use for images.

2.1. Multifractal spectrum

Let $X(\mathbf{t}) : t \in \mathbb{R}^d \to X \in \mathbb{R}$ denote the function to be analyzed, assumed to belong to the space of bounded functions. For an image, $d = 2$ and the variable $\mathbf{t} = (x_1, x_2)$ is commonly referred to as the *space* variable. MA consists in describing the local regularity of $X(\mathbf{t})$, around $\mathbf{t}_0$ by comparing $X(\mathbf{t}_0)$ against a local power law behavior: $|X(\mathbf{t}) - P_{\mathbf{t}_0}(\mathbf{t})| \leqslant C|\mathbf{t} - \mathbf{t}_0|^\alpha$, with $\alpha > 0$, and where $C > 0$ and P is a polynomial such that $deg(P) < \alpha$. The Hölder exponent $h(\mathbf{t}_0)$ is the largest such exponents α. The fluctuations of h with respect to $\mathbf{t}$ are usually described via the *multifractal spectrum*. It collects the Hausdorff dimensions of the sets of positions $\mathbf{t}$, for which the Hölder exponents take the same value : $\mathscr{D}(h) = \dim_H\{\mathbf{t} : h(\mathbf{t}) = h\}$. Because of its being a Hausdorff dimension, the multifractal spectrum is confined to $0 \leqslant \mathscr{D}(h) \leqslant d$. By convention, $\mathscr{D}(h) = -\infty$ for the Hölder exponents that are not present in X. For theoretical introductions to MA, the reader is referred to e.g., [17,18].

If X is a bounded function, its Hölder exponent is necessarily non-negative, so that $\mathscr{D}(h) = -\infty, \forall h < 0$. For ease of exposition, we hereafter only consider images that are *uniformly singular*, which implies that the Hölder exponent is bounded from above, see [26]. From a practical point of view, MA consists in estimating $\mathscr{D}(h)$ from the finite size image under analysis. This is commonly achieved via the so-called *multifractal formalisms*. The WL MA is defined in the next section.

2.2. Wave leader multifractal analysis

Wavelet coefficients: Let $H_0(k)$, $G_0(k)$ denote the (low-pass and high-pass, respectively) quadrature mirror filters defining a 1D orthonormal DWT. The underlying mother wavelet possesses $N_\psi \geqslant 1$ vanishing moment(s). A 2D orthonormal DWT can be defined via the use of four bi-dimensional filters $G^{(m)}(k_1, k_2)$, $m = 0, 1, 2, 3$ obtained as products of H_0 and G_0. By convention, $G^{(0)}(k_1, k_2) = H_0(k_1)H_0(k_2)$ corresponds to the 2D low-pass filter providing a lower approximation, while $G^{(m)}$, $m = 1, 2, 3$, correspond to the high-pass filters yielding the wavelet coefficients. Let $\{X(k_1, k_2), k_1 = 1, \ldots, N_1, k_2 = 1, \ldots, N_2\}$ denote the 2D gray level digitized image to be analyzed, regarded as a sampled version of $X(x_1, x_2)$. The 2D wavelet coefficients $D_X^{(m)}(j, k_1, k_2)$, $m = 1, 2, 3$, are obtained by, first ($j = 1$), convolution of $G^{(m)}(k_1, k_2)$, $m = 0, 1, 2, 3$ with $\{X(k_1, k_2)\}$ and down-sampling, and then ($j \geqslant 2$) iterative convolution of $G^{(m)}(k_1, k_2)$, $m = 0, 1, 2, 3$ with $D_X^{(0)}(j - 1, k_1, k_2)$ and down-sampling. For detailed introduction to continuous time and discrete time 1D or 2D WT, the reader is referred to, e.g., the tutorial books [19,27].

For scaling analysis, it is more suitable (cf. [12,13]) to re-normalize the standard L^2-norm wavelet coefficients according to a L^1-norm: $d_X^{(m)}(j, k_1, k_2) = 2^{-jd/2}D_X^{(m)}(j, k_1, k_2)$.

Wavelet leaders: Let us now further assume that the $H_0(k)$, $G_0(k)$ have finite impulse responses, and introduce a dyadic indexing of squares as

$$\lambda_{j,k_1,k_2} = \{[k_1 2^j, (k_1 + 1)2^j), [k_2 2^j, (k_2 + 1)2^j)\}.$$

The union of nine such neighbor intervals is denoted as

$$3^2 \lambda_{j,k_1,k_2} = \bigcup_{n_1,n_2=\{-1,0,1\}} \lambda_{j,k_1+n_1,k_2+n_2}.$$

WLs are theoretically defined by

$$L_X(j, k_1, k_2) = \sup_{m=1,2,3, \lambda' \subset 3^2\lambda_{j,k_1,k_2}} |d_X^{(m)}(\lambda')| \tag{1}$$

(see [17]). This definition is illustrated in Fig. 1 and practically means that the leader $L_X(j, k_1, k_2)$ is obtained as the largest wavelet coefficient amongst those, $|d_X^{(m)}(j', k_1', k_2')|$, $m = 1, 2, 3$, existing in a (narrow) spatial neighborhood of (k_1, k_2), at any finer scale $2^{j'} \leqslant 2^j$.

The central result underlying the use of WLs for MA lies in them accurately measuring local Hölder exponents (cf. [17] for the theoretical proof): if X has Hölder exponent $h(\mathbf{t}_0) \geqslant 0$ in $\mathbf{t}_0$, then, on condition that $N_\psi > h(\mathbf{t}_0)$ and, if $2^{-j}\mathbf{k}$ is the dyadic point of scale j which is closest to $\mathbf{t}_0$

$$L_X(j, \mathbf{k}) \sim_{2^j \to 0} 2^{jh(\mathbf{t}_0)}, \tag{2}$$

where $X_a \sim_{a \to 0} Y_a$ means that both quantities share the same lim inf on a log–log scale.

Structure functions and scaling: Let us now form the *structure functions*, i.e., spatial averages of (the q-th order of) the leaders at a given scale 2^j:

$$S(2^j, q) = \frac{1}{n_j} \sum_{k_1,k_2} L_X(j, k_1, k_2)^q. \tag{3}$$
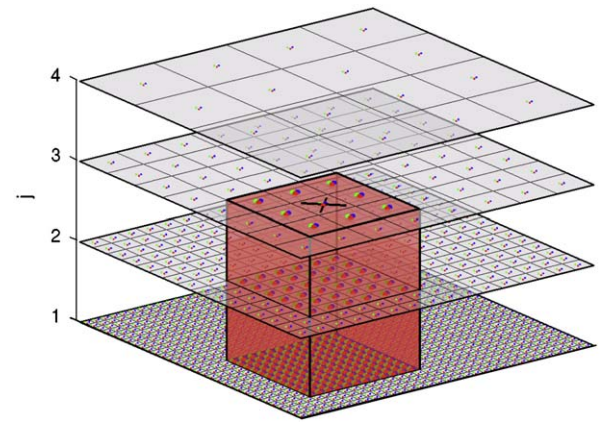
Fig. 1. *Definition of wavelet leaders*. The wavelet leader $L_X(j, k_1, k_2)$ at scale 2^j and position (k_1, k_2) (black cross) is defined as the largest of the wavelet coefficients $|d_X^{(m)}(j', k_1', k_2')|, m = 1, \ldots, 3$ (red, green and blue dots) within a spatial neighborhood of (k_1, k_2) and within all finer scale $2^{j'} \leqslant 2^j$ (red volume). The wavelet coefficients over which the supremum is taken are marked by fat dots. (For interpretation of the references to color in the figure legend, the reader is referred to the web version of this article.)

The scaling function $\zeta(q)$ is then defined as

$$\zeta(q) = \lim_{2^j \to 0} \inf \frac{\ln S(2^j, q)}{\ln 2^j}. \tag{4}$$

In practice, this definition means that the $S(2^j, q)$ exhibit power law behaviors with respect to the analysis scale 2^j, in the limit of small scales $2^j \to 0$ [14]:

$$S(2^j, q) \sim \lambda_q 2^{j\zeta(q)} \quad \text{when } j \to -\infty. \tag{5}$$

The $\zeta(q)$ are hence often termed the *scaling exponents*. This power law behavior establishes a clear and deep connection between the concepts of scale invariance and MA. Eq. (4) also implies that the scaling function necessarily is a concave function of q [14].

Multifractal formalism: Let $\mathscr{L}(h)$ be the *Legendre spectrum* defined from the scaling function through a Legendre transform:

$$\mathscr{L}(h) = \inf_{q \in \mathbb{R}} (d + qh - \zeta(q)). \tag{6}$$

Under a mild uniform regularity condition for X (uniform Hölder, cf. Section 3.2), it can be shown [14,17] that the Legendre spectrum and the multifractal spectrum are simply related : $\mathscr{D}(h) \leqslant \mathscr{L}(h)$. There exist (large) classes of functions and processes $X(\mathbf{t})$ for which this inequality turns to an equality, referred to as the WL based *multifractal formalism*:

$$\mathscr{D}(h) = \mathscr{L}(h). \tag{7}$$

Notably, for the self-similar and multiplicative cascade processes used in the present contribution to evaluate the statistical properties of the proposed estimation procedures (cf. Section 5), the WL multifractal formalism holds. An obvious necessary condition for it to hold is that the spectrum $\mathscr{D}(h)$ of $X(\mathbf{t})$ is a concave function. In practice, one cannot have access to the spectrum of singularities of a real-life signal; therefore the purpose of practical MA focuses on the estimation of the Legendre spectrum $\mathscr{L}(h)$.

Cumulant expansion: Let us now assume that the scaling exponents $\zeta(q)$ are a smooth function of q around 0; then, we can consider a Taylor expansion of this scaling exponents at $q = 0$:

$$\zeta(q) \simeq \sum_{p \geqslant 1} c_p q^p / p!. \tag{8}$$

It has been shown in [28,29] that the *log-cumulants* c_p are related to the cumulant of order p, $C(2^j, p)$, of $\ln L_X(j, \mathbf{k})$ as

$$C(2^j, p) = c_{0,p} + c_p \ln 2^j. \tag{9}$$

The concavity of $\zeta(q)$ implies that $c_2 \leqslant 0$. Recently, we showed (detailed calculations reported in [30]) that Eq. (8) can be cast into a polynomial expansion of the spectrum as

$$\mathscr{L}(h) = d + \frac{c_2}{2!} \left(\frac{h - c_1}{c_2}\right)^2 + \frac{-c_3}{3!} \left(\frac{h - c_1}{c_2}\right)^3 + \frac{-c_4 + 3c_3^2/c_2}{4!} \left(\frac{h - c_1}{c_2}\right)^4 + \cdots . \tag{10}$$

This indicates that c_1 corresponds to the location of the maximum of $\mathscr{L}(h)$, c_2 to its width, while c_3 is an asymmetry parameter. In applications, practitioners can-

not compute the entire functions $\zeta(q)$ or $\mathscr{L}(h)$ and instead often concentrate on a small number of well chosen representative multifractal attributes. The c_p are candidates of particular interest and one usually computes c_1 and c_2 and, when data permit, c_3. This is further discussed in Section 6 for the specific context of image analysis.

2.3. Estimation procedures

For images, estimation of the scaling or multifractal attributes can be conducted as in the 1D case, mutatis mutandis. Estimation procedures have been described at length in [22,25] and are only briefly outlined here. As suggested by Eqs. (5) and (8), the estimation of the $\zeta(q)$ and of the c_p can be performed by means of linear regressions:

$$\hat{\zeta}(q) = \sum_{j=j_1}^{j_2} w_j \log_2 S(2^j, q), \tag{11}$$

$$\hat{c}_p = (\log_2 e) \cdot \sum_{j=j_1}^{j_2} w_j \hat{C}(2^j, p), \tag{12}$$

where the estimates $\hat{C}(2^j, p)$ for the cumulants of $\ln L_X(j, \cdot)$ are obtained from standard sample cumulant estimators. The weights w_j have to satisfy the constraints $\sum_{j_1}^{j_2} j w_j \equiv 1$ and $\sum_{j_1}^{j_2} w_j \equiv 0$ and can be expressed as $w_j = b_j(V_0 j - V_1)/(V_0 V_2 - V_1^2)$ with $V_i = \sum_{j_1}^{j_2} j^i b_j, i = 0, 1, 2$. The freely selectable positive numbers b_j reflect the confidence granted to each $\hat{C}(2^j, p)$ or $\log_2 S(2^j, q)$. To estimate $\mathscr{L}(h)$, it has been proposed [31] to handle practically the Legendre transform via its parametric form, $h(q), L(q)$. Such a formulation efficiently matches the bootstrap requirements for confidence interval derivation (cf. Section 4) and is hence used here. Tedious yet simple calculations lead to the following estimators:

$$\hat{h}(q) = \sum_{j=j_1}^{j_2} w_j V(2^j, q), \quad \hat{L}(q) = \sum_{j=j_1}^{j_2} w_j U(2^j, q), \tag{13}$$

where

$$V(j, q) = \frac{\sum_{k=1}^{n_j} L_X^q(j, k) \log_2 L_X(j, k)}{n_j S(j, q)}$$

and

$$U(j, q) = \frac{\sum_{k=1}^{n_j} L_X^q(j, k)(\log_2 L_X^q(j, k) - \log_2 n_j S(j, q))}{n_j S(j, q)} + \log_2 n_j.$$

2.4. Wavelet coefficients versus leaders

Empirical scaling or multifractal analysis for images has so far been mostly conducted using a MA based directly on the wavelet coefficients of a 2D DWT. The corresponding structure functions are computed as

$$S^d(2^j, q) = \frac{1}{3n_j} \sum_{m=1}^{3} \sum_{k_1, k_2} |d_X^{(m)}(j, k_1, k_2)|^q. \tag{14}$$

The remainder of the formalism (Eqs. (5)–(10)) and of the estimation procedures (Eqs. (11)–(13)) can be obtained by replacing $L_X(j, \mathbf{k})$ with $|d_X(j, \mathbf{k})|$ (and similarly for the bootstrap procedures defined in Section 4).

As pointed out earlier in Section 1, the wavelet coefficient MA suffers from a major theoretical drawback: a complete MA cannot be conducted, as negative q structure functions are numerically unstable and diverge because wavelet coefficients are mostly concentrated around the 0 value, see [14] where a precise mathematical analysis of this phenomenon is carried out for some classes of stochastic processes. The WL MA is designed to overcome this difficulty and benefits from two other key theoretical properties: it is proven to be valid for self-similar and multiplicative cascade processes (while the wavelet coefficient MA holds only partially, and for a restricted class), and the scaling exponents $\zeta(q)$ are shown not to depend on the precise choice of the wavelet[1] H_0, G_0 [14,17]. In Section 6, we further compare (very favorably) the leader based MA to the wavelet coefficient based one both in terms of practical estimation performances and bootstrap based confidence interval derivation.

However, an important limitation of the WL based MA results from the fact that it can be directly applied only to bounded functions, while the wavelet coefficient MA is not restricted to this class.

This question, together with a number of related theoretical issues of importance for a practical use of MA on real images, is further addressed in the next section.

3. Advanced considerations on multifractal analysis of images

As mentioned in Section 1, there is a priori no guarantee that actual digital images are the discretization of a function that belongs to an $L^q(\mathbb{R}^2)$ space, $q \geqslant 1$, (or, a fortiori, belongs to the space of bounded variation (BV) functions, i.e., functions whose gradient is a bounded measure). Along the same line, one can hardly decide a priori whether the images under analysis fall within the class of bounded functions, permitting a straightforward application of the leader MA. Indeed, scanning large image databases (such as the one reported in [11]) confirms that there are roughly as many images which are bounded as images which are unbounded (see in Section 3.2 how this can be practically determined on discretized signals). Hence, the leader based MA cannot be applied to images without prior checking.

Note that the violation of the bounded function requirement can be related to the existence of negative Hölder exponents in the data (see Section 3.2), and it is indeed commonly reported in the literature dedicated to empirical MA that images exhibit negative Hölder exponents [32]. There is no general consensus on a precise mathematical definition of negative Hölder exponents, and a discussion of this notion requires theoretical developments beyond the scope of this contribution (this is addressed in [33,34]); we can, however, indicate that the underlying heuristic remains yet the same: in some averaged sense, $|X(\mathbf{t}) - X(\mathbf{t_0})| \sim_{|\mathbf{t}-\mathbf{t_0}| \to 0} |\mathbf{t} - \mathbf{t_0}|^h$.

These involved issues have been partially addressed in [33] and are further elaborated in this section. Furthermore, the analyses reported here indicate that, though wavelet coefficients offer a restricted analysis of the multifractal properties of an image, a number of useful information can still be extracted from the wavelet coefficient based structure functions.

3.1. Images and function space models

Let us define, for $q > 0$,

$$\zeta^d(q) = \lim_{2^j \to 0} \inf \frac{\ln S^d(2^j, q)}{\ln 2^j}. \tag{15}$$

Then, $\zeta^d(q) > 0$ indicates that the image X belongs to $L^q(\mathbb{R}^2)$. Indeed, the wavelet characterization of the Sobolev spaces $L^{q,s}$ implies that

$$\text{if } q \geqslant 1 \quad \text{then } \zeta^d(q) = \sup\{s : f \in L^{q,s/q}\},$$

see [26]; therefore $\zeta^d(q) > 0$ implies that f belongs to a Sobolev space $L^{q,s}$ for an $s > 0$; a fortiori, it belongs to $L^{q,0}$, which coincides with the space L^q. For $q = 2$, this provides the practitioners with tools helping to decide whether or not X fits the assumptions of the Osher–Rudin–Fatemi model [38]. This remark is not only pertinent for this model: all other models which have been later proposed as alternatives (see for instance the book of Meyer [35] and references therein, or [36]) are based on the hypothesis that the image considered belongs to a given function space (or a sum of function spaces). Since all the function spaces which have been proposed in this context either are Sobolev spaces or satisfy sharp embeddings with Sobolev spaces, it follows that the determination of the wavelet scaling function of a given image allows to determine if it satisfies a particular function space assumption, and, therefore, if the corresponding algorithm can be reasonably applied in this case. When $q = 1$, the same argument as above yields that, if $\zeta^d(1) > 0$, then X belongs to $L^1(\mathbb{R}^2)$ and additionally, $\zeta^d(1) > 1$ implies that X belongs to the class of BVs images. Furthermore, X is a measure necessarily yields $\zeta^d(1) \geqslant 0$.

Scanning image databases reveals that a non-negligible proportion of images (e.g., $\approx 10\%$ for the Univ. of Maryland data set (cf. www.cfar.umd.edu/users/fer/website-texture/texture.htm) are characterized with $\zeta^d(2) < 0$, with confidence intervals (computed with the technique proposed in Section 4) clearly validating the negativity for the estimate. Also, $\zeta^d(1)$ is positive for most images (as expected for positive measures), yet that $0 < \zeta^d(1) < 1$ for a large proportion of images (e.g., $\approx 90\%$ for the Univ. of Maryland data set), which are hence not within the BV class.

For illustration purpose, the image used in Section 6.4 (cf. Fig. 7) is characterized by $\zeta^d(1) = -0.08 \pm 0.03$ and $\zeta^d(2) = -0.17 \pm 0.08$, confidence intervals being obtained with the bootstrap approach described in Section 4.

---

[1] A precise mathematical statement of this result requires further elaboration beyond the scope of this contribution, see e.g., [14,17].

3.2. Uniform regularity

A measure or a function $X(\mathbf{t})$ is said to belong to C^ε, $\varepsilon \in \mathbb{R}$, when its wavelet coefficients satisfy

$$\exists C > 0 : \forall j, k_1, k_2, m |d_X^{(m)}(j, k_1, k_2)| \leqslant C 2^{j\varepsilon}. \tag{16}$$

A uniform regularity exponent can hence be defined by

$$h_{min} = \sup\{\varepsilon : X \in C^\varepsilon\}. \tag{17}$$

A function or a measure is said to be *uniformly Hölder* if $h_{min} > 0$. In turns, $h_{min} > 0$ implies that

$$\forall t_0, h(\mathbf{t}_0) \geqslant h_{min},$$

and also that X is a continuous function, hence bounded, hence possesses finite WLs in the limit of fine scales (all implications are strict).

As stated in Section 2.2, the computation of WLs, hence the computation of the Legendre spectrum is possible only for functions which are uniformly Hölder. Applied to images that do not respect this restriction, the WL based MA produces results that are meaningless. However, one can meet the following pitfall: in practice, any image will yield empirical WLs with finite value (because the supremum in the definition of WLs (1) is in practice always taken on a finite set), independently of the fact that h_{min} is positive or not. Hence, practitioners have little or no means to decide a posteriori whether leaders are meaningful or not and this needs to be checked a priori. A sufficient condition is that the image is *uniformly Hölder* and hence that $h_{min} > 0$. This can be evaluated via the formulation:

$$h_{min} = \lim_{2^j \to 0} \inf \frac{\ln \sup_{m,k_1,k_2} |d_X^{(m)}(j, k_1, k_2)|}{\ln 2^j}, \tag{18}$$

which is a direct consequence of Eq. (16) and practically amounts to performing linear regressions of the log of the magnitudes of the largest wavelet coefficients at scales 2^j versus log of scales. The performances of this estimator, assessed over 500 realizations of a synthetic multifractal stochastic images of size 1024×1024 (cf. Section 5.3) is summarized in Table 1. The results clearly demonstrate that estimation of the uniform regularity exponent is feasible from a standard size image.

Examination of image databases shows that images are found as often with negative h_{min} as with positive one (e.g., $\approx 50\%$ for Univ. of Maryland data set). For a simple illustration purpose, the image used in Section 6.4 (cf. Figs. 7 and 8) is characterized by $h_{min} = -0.24$. This calls

Table 1
Estimation of h_{min}.

h_{min} CMC-LP			
Theory	mean	std	mse
−0.391	−0.395	0.117	0.117

Mean, standard deviation and root mean squared error (cf. Eq. (27)) of wavelet coefficient based estimation of h_{min} (Eq. (18)) for CMC-LP, obtained by numerical simulation as described in Section 5.3 with linear regressions over the finest scales $2^1 \leqslant 2^j \leqslant 2^3$. The column on the left states the theoretical value of h_{min}.

for a modification of the leader based MA proposed in Section 2.2 for bounded functions. This is the subject of the next section.

3.3. Fractional integration

To overcome the negative h_{min} issue, it has been proposed to fractionally integrate with an order larger than $-h_{min}$, which implies that the uniform regularity exponent of the new image is positive, and thus insures that all Hölder exponents are positive. This has been for instance abundantly used in [8,20,39].

The fractional integration (of order η) of a function or measure X is defined in the Fourier domain as

$$(\widehat{I^\eta X})(\xi) = (1 + |\xi|^2)^{\eta/2} \hat{X}(\xi). \tag{19}$$

If X is such that $h_{min} \leqslant 0$, then $I^\eta X$ is a uniformly Hölder function as soon as

$$\eta > -h_{min}; \tag{20}$$

this result is a direct consequence of the interpretation of h_{min} in terms of the Lipschitz spaces $C^\alpha(\mathbb{R}^n)$:

$$h_{min} = \sup\{\alpha : X \in C^\alpha(\mathbb{R}^n)\},$$

and of the fact that if $X \in C^\alpha$, then $\widehat{I^\eta X} \in C^{\alpha+\eta}$. Indeed, it follows that if $\eta > -h_{min}$, then $\widehat{I^\eta X}$ belongs to C^ε for an $\varepsilon > 0$, hence is a bounded function, see [34] for details.

Instead of actually computing the fractionally integrated version of X and then applying the WL multifractal formalism to it, both operations can be combined into a single one, as follows:

(i) First compute the 2D WT coefficients $d_X^{(m)}(j, k_1, k_2)$ and replace them with

$$d_X^{(m),\eta}(j, k_1, k_2) = 2^{\eta j} d_X^{(m)}(j, k_1, k_2).$$

This amounts to computing the wavelet coefficients of $I^\eta X$, a pseudo-fractionally integrated version of X, whose local and global regularity properties are identical to that of $I^\eta X$, as soon as $\eta > -h_{min}$, see [34].

(ii) WLs are computed from these new wavelet coefficients:

$$L_X^\eta(j, k_1, k_2) = \sup_{m,\lambda' \subset 3\lambda_{j,k_1,k_2}} |d_X^{(m),\eta}(\lambda')|. \tag{21}$$

Such modified leader coefficients are equivalent to those computed from $I^\eta X$, in the sense that if $I^\eta X$ has Hölder exponent h at $\mathbf{t}_0$ then, when $2^{-j}\mathbf{k}$ is the closest dyadic point of t_0, $L_X^\eta(j, k_1, k_2) \sim 2^{jh}$.

(iii) Compute new structure functions:

$$S_\eta(j, q) = \frac{1}{n_j} \sum_{k_1, k_2} L_X^\eta(j, k_1, k_2)^q. \tag{22}$$

They behave as power laws with respect to the analyzing scale 2^j, in the limit of fine scales $2^j \to 0$:

$$S_\eta(j, q) \approx G_q^\eta 2^{j\zeta_\eta(q)}, \tag{23}$$

yielding the multifractal spectrum of $I^\eta X$:

$$\mathscr{L}_\eta(h) = \min_{q \neq 0}(1 + qh - \zeta_\eta(q)). \tag{24}$$

One can prove that the scaling function (and therefore the Legendre spectrum) thus obtained is the same one as if a "true" fractional integration had been performed, see [34]. Note that Condition (20) does not prescribe a unique value for η. Therefore one meets the following alternative:

- A thorough possibility consists in computing the Legendre spectra $\mathscr{L}_\eta(h)$ for a wide range of values of η, and using this collection of spectra for classification, or in order to understand the nature of the pointwise singularities of X. Preliminary results in this direction are given in [34].
- A simpler option consists in noticing that, for large classes of mathematical functions and stochastic processes, one can prove that all the functions $\mathscr{L}_\eta(h + \eta)$ are actually the same, and therefore define a unique function $\mathscr{L}(h)$:

$$\forall \eta > -h_{min}, \quad \mathscr{L}(h) = \mathscr{L}_\eta(h + \eta). \tag{25}$$

A precise analysis of the validity of Eq. (25) is beyond the scope of this paper and can be found in [34,36]; let us just mention that it is related to the absence of strongly oscillating features in the image, such as the ones provided by *chirps* of the form $|x - x_0|^\alpha \sin(|x - x_0|^{-\beta})$. Note, however, that some classical models do not satisfy Eq. (25); typical examples are supplied by *lacunary wavelet series*, see [37]. If Eq. (25) holds, then the particular value of η which is picked is irrelevant (as soon as it is large enough): in practice, one picks one value of η and defines the Legendre spectrum by Eq. (25); the MA is performed using this function $\mathscr{L}(h)$ for spectrum.

Though this second option is successfully used for classification in a number of applications, it is important to be aware that this heuristic faces limitations: besides the problem of the validity of Eq. (25) which has already been mentioned, the function $\mathscr{L}(h)$ cannot generally be related to the multifractal properties of X. Nonetheless, it is deeply related to the intrinsic properties of the original image X and can be used as such (for classification, for instance).

Finally, note that fractional integration also increases the $\zeta^d(q)$ (the counterpart of the heuristic translation in Eq. (25) reads $\zeta_\eta^d(q) = \zeta^d(q) + \eta q$), hence ensuring, for large enough η, that $\zeta_\eta^d(1) > 1$ and/or $\zeta_\eta^d(2) > 0$.

3.4. Validity of the multifractal formalism

It is also of importance to be aware that theoretically Eq. (7) does not hold in general. More precisely, let us assume that X belongs to the class of *mild functions*, defined as $\exists C_1, C_2, A, B > 0$ such that $\forall j, k, C_1 2^{jA} \leqslant L_X(j, \mathbf{k}) \leqslant C_2 2^{jB}$ (this implies that X is nowhere C^∞, but satisfies a minimal uniform regularity assumption). When X is a *mild* function, its $\zeta(q)$ is an *admissible* function, i.e., it satisfies:

(i) $\zeta(0) = 0$,
(ii) $\zeta(q)$ is concave and increasing on $\mathbb{R}$,
(iii) $0 \leqslant \zeta(q) - q\zeta(q)/dq \leqslant d$.

Conversely, one can show [26] that any admissible function corresponds to the $\zeta(q)$ of a *mild* function X. However, this does not ensure that X satisfies the WL multifractal formalism. Let, for instance, $\lambda(q)$ be an admissible function. One can design the following *trifractal* function whose $\zeta(q) = \lambda(q)$: it is constructed such that its multifractal spectrum reads $\mathscr{D}(h_{min}) = \mathscr{D}(h_{max}) = 0$, $\mathscr{D}(h_{med}) = d$ and $\mathscr{D}(h) = -\infty$ elsewhere, with $h_{med} = \zeta'(0)$, $h_{min} = \zeta'(+\infty)$, and $h_{max} = \zeta'(-\infty)$. As soon as these three values $h_{min}, h_{med}, h_{max}$ differ, the multifractal formalism (as in Eq. (7)) obviously ceases to hold, since the Legendre transform of $\zeta(q)$ is a concave function. Another counterexample is detailed in [26] where the generality of the validity of the multifractal formalism is further investigated.

3.5. Wavelet coefficients versus leaders

This section leads to the conclusion that wavelet coefficients are providing preliminary information regarding the regularity properties of X and should hence be used prior to applying the WL MA, and in a complementary manner, rather than with the usual competition perspective.

4. Space-scale block bootstrap

We now extend the line of work proposed in [22,25] for the design of bootstrap confidence limits for 1D multifractal processes (signals) to 2D ones (images). While most scale invariant processes are characterized by difficult statistical properties (non-stationary, intricate dependence), their wavelet coefficients often form stationary sequences with less involved dependence structure [22]. Therefore, it is more natural to apply bootstrap schemes in the wavelet domain rather than in the space one. We devise a specific construction of space-scale blocks to ensure that the residual dependencies of leaders, both in space and in scale, are approximately reproduced by the bootstrap resamples. Also, these space-scale blocks ensure that bootstrapped WLs preserve their key property for MA, namely Eq. (2).

For an overview of bootstrap and bootstrap methods for dependent data, see e.g., [23,40,41].

4.1. Space-scale blocks of wavelet leaders

For ease of notation and without loss of generality, we assume square images ($N_1 = N_2 = N$). The space-scale blocks of leaders are defined as 3D boxes, extending over all scales, with a square base of a fixed number of pixels. All leaders lying within such a box form one space-scale block. The blocks are constructed overlapping and on circularized leaders, i.e., on $L_X^c(j, k_1, k_2) = L_X(j, k_1 \bmod n_j, k_2 \bmod n_j)$, such that each leader has the same probability to be within a resample. More precisely, the collection of leaders $L_X(j', k_1', k_2')$ that form a space-scale block $\mathscr{I}(k_1, k_2)$, of $2l \times 2l$ pixels, located at position (k_1, k_2), is given by (cf. Fig. 2)

$$\mathscr{I}(k_1, k_2) = \{L_X(j', k_1' \bmod n_{j'}, k_2' \bmod n_{j'}):$$
$$|k_1 - k_1' 2^{j'}| \leqslant l, |k_2 - k_2' 2^{j'}| \leqslant l, 1 \leqslant j' \leqslant j_{max}\}. \tag{26}$$
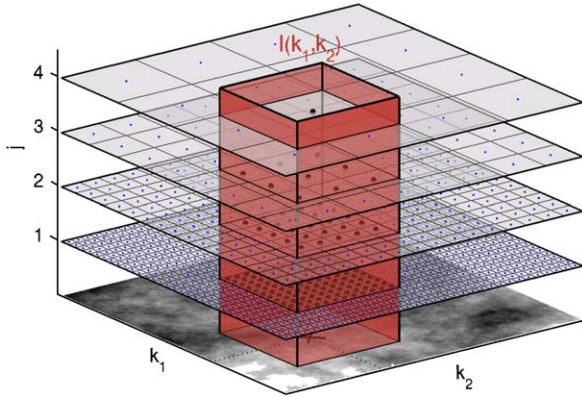
Fig. 2. *Space-scale block construction.* The space-scale block of leaders $\mathscr{I}(k_1, k_2)$ at position (k_1, k_2) consists of the collection of leaders (fat black dots) that are within a box with square base of base length $2l$, centered at (k_1, k_2) and extending over all scales (red volume).
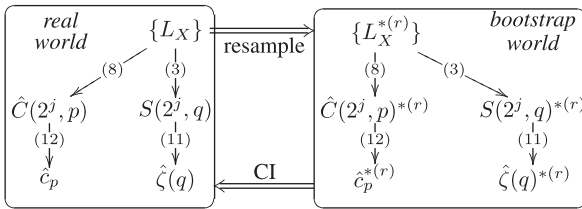
Fig. 3. *Estimation and bootstrap estimation procedures.* Overview of estimation procedure (left) and bootstrap estimation procedure (right). 'Resample' corresponds to the space-scale block bootstrap resampling procedure described in Section 4, "CI" to confidence limit calculation from empirical bootstrap distributions as in Section 4.3, and (·) on arrows indicates the equation involved in estimation. The scheme can be written equivalently for $\hat{D}(q)$ and $\hat{h}(q)$.

4.2. Bootstrap resampling and estimation

Each single bootstrap resample of leaders $\mathscr{L}_X^{*(r)}, r = 1, \ldots, R$, is obtained as follows. First, $B = \lceil N/2l \rceil$ blocks of leaders $\mathscr{I}^*(k_1, k_2)$ are drawn at random, independently and with replacement, from the available blocks $\mathscr{I}(k_1, k_2), k_1, k_2 = 1, \ldots, N$. Then, blocks are concatenated in space, such that each resampled leader remains located at its original scale 2^j.

The bootstrap estimation procedure re-applies the estimation procedure described above to each of this bootstrap resamples $\mathscr{L}_X^{*(r)}$: First, the bootstrap structure functions $S(2^j, q)^*$ and $C(2^j, q)^*$ are obtained by applying Eqs. (3) and (8). Then, bootstrap estimates $\hat{\zeta}(q)^*$, $\hat{D}(q)^*$, $\hat{h}(q)^*$ and $\hat{c}_p^*$ are calculated as in Eqs. (11), (13) and (12). These estimation and bootstrap estimation procedures are sketched in Fig. 3. Note that the bootstrap resampling and estimation procedures can as well be applied directly to wavelet coefficients instead of leaders.

4.3. Bootstrap confidence limits

For parameters $\theta \in \{\zeta(q), D(q), h(q), c_p\}$, we use the equitailed $(1 - \alpha)$ bootstrap percentile confidence interval, defined as $\hat{CI}_\theta = [\hat{\theta}_{\alpha/2}^*, \hat{\theta}_{1-\alpha/2}^*]$, where $\hat{\theta}_\alpha^*$ is the α quantile of

the empirical distribution of $\hat{\theta}^*$ obtained by the bootstrap estimation procedure described above. Double bootstrap estimates could be obtained and used for more sophisticated confidence limit and hypothesis test constructions, such as studentized or adjusted confidence limits and tests. Such issues have been considered in [22,25] for the 1D case. An extension to images is currently investigated.

5. Performance assessment on synthetic multifractal images

5.1. Methodology: Monte Carlo simulations

We assess the performances of the proposed estimation procedures by applying them to a large number N_{MC} of realizations of synthetic stochastic 2D processes of size $(N \times N)$ with a priori known and controlled multifractal properties. The aim of the numerical study is to address the following issues: Do the estimation procedures exhibit satisfactory statistical performance? Should one prefer wavelet coefficients or leaders for the estimation of multifractal attributes of images? Are the bootstrap confidence limits reliable, i.e., do they reproduce targeted coverages?

5.2. Synthetic multifractal processes

We use two stochastic processes: fractional Brownian motion (FBM) and canonical Mandelbrot's multiplicative cascade with log-Poisson multipliers (CMC-LP). They provide us with simple yet representative examples of Gaussian monofractal processes and multifractal processes, respectively. Example of such fields are shown in Fig. 4.

FBM : We use the 2D Gaussian self-similar FBM, as defined in [42]. Its statistical properties are completely determined by a single parameter, the Hurst exponent H. FBM has scaling properties as in Eq. (5), with $\zeta(q) = qH$ and therefore $c_1 = H$, $c_p \equiv 0, p \geqslant 2$. Its multifractal spectrum reduces to one single point $h = H$ where $\mathscr{D}(H) = 2$, hence, FBM is monofractal.

CMC-LP: The multiplicative cascades of Mandelbrot (cf. [43]) have for long been the only example of multifractal processes practically available. Their construction is based on an iterative split-and-multiply procedure on an interval. In this work, we use a binary cascade and log-Poisson multipliers $s = 2^\gamma \exp(\ln(\beta)\pi_\lambda)$, where π_λ is a Poisson random variable with parameter $\lambda = -\gamma \ln(2)/(\beta - 1)$. To handle negative minimum regularity, the cascade is (pseudo) fractionally integrated (according to the procedure described in Section 3.3), with a parameter $\eta > 0$. The CMC-LP are multifractal with $\zeta(q) = (\eta - \gamma)q + \gamma(\beta^q - 1)/(\beta - 1)$, $c_1 = \eta + \gamma(\ln(\beta)/(\beta - 1) - 1)$ and $c_p = -\gamma/(\beta - 1)(-\ln(\beta))^p$, $\mathscr{D}(h) = 2 + \gamma/(\beta - 1) + (-\eta + \gamma + h)/\ln\beta \cdot [\ln((-\eta + \gamma + h)(\beta - 1)/\gamma \ln\beta) - 1]$.

5.3. Simulation setup

Results are reported here with one specific selection of process parameter settings. Similar results have been
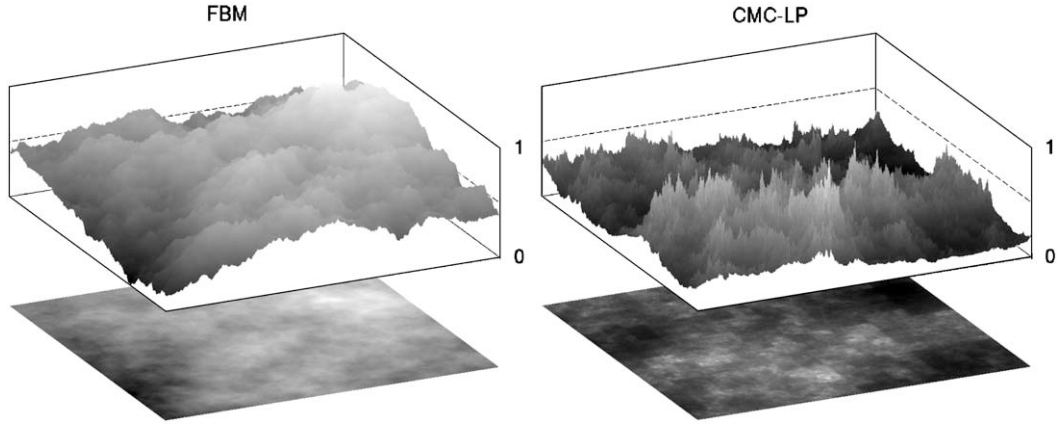
Fig. 4. *Synthetic processes.* One realization of FBM (left) and of CMC-LP (right). The bottom plane presents the images, the axes on top an amplitude view of the images (amplitudes normalized to [0,1]), illustrating the (ir)regularity of the images.

obtained for a range of different process parameters, and are not reported here for space reasons. Parameters for numerical simulations are set to $N_{MC} = 500$ and $N = 1024$. All results are obtained with Daubechies' wavelets with $N_\psi = 2$ vanishing moments. It has been checked that using wavelets with larger N_ψ yields identical results and conclusions. Linear regressions are performed over the scales $2^3 \leqslant 2^j \leqslant 2^7$ with weights $b_j = n_j$, as proposed in [22]. We use $R = 99$ bootstrap resamples and block lengths $l = 85$ (FBM) and $l = 128$ (CMC-LP). The target significance for bootstrap confidence limits is set to 90%. The process parameters are fixed to $H = 0.7$ for FBM, and $\beta = 0.84$, $\gamma = 0.42$, $\eta = 0.5$ for CMC-LP, such that $[c_1, c_2, c_3] = [0.538, -0.080, 0.014]$.

6. Results

6.1. Structure functions

Fig. 5 shows, for FBM (left) and CMC-LP (right), means over Monte Carlo realizations of structure functions $\log_2 S(2^j, q)$ for $q = 2$ (top row) and for $q = -2$ (second row), and the deviations of the structure functions from their theoretical slope, $\log_2 S(2^j, q) - j\zeta(q)$, for $q = 2$ (third row) and $q = -2$ (bottom row). The 95% asymptotic confidence limits are obtained by Monte Carlo simulation. As structure functions for wavelet coefficients diverge for negative q's, only positive q's are shown.

Scaling range: A first investigation (top and second row) suggests that for both wavelet coefficients and leaders, structure functions display scaling behavior as in Eq. (5) over the range of scales $2^2 \leqslant 2^j \leqslant 2^7$. A closer look at the deviations from the theoretical slope (third and last row) confirms this observation for coefficients. However, it reveals that for leaders, $\log_2 S(2^j, q)$ becomes a linear function of j only for $2^j \geqslant 2^3$. This can be explained by the fact that, theoretically, a leader is defined as the sup of coefficients at all finer scales down to infinitely fine scales, whereas practically, the sup can be taken only down to the finest available, first scale. Hence, in practice, leaders need one or two scales for initialization, whereas coefficients do not.

Projection step: The non-scaling behavior of $S(2^j, q)$ for wavelet coefficients at the first scale $j = 1$ is due to the fact that the pre-filtering or projection step theoretically necessary for a clean wavelet analysis has been omitted (cf. [44]).

Regressions: We observe further that the error bars for structure functions for CMC-LP are substantially larger than those for FBM, suggesting a smaller variability of the $S(2^j, q)$ and better subsequent estimation performances for the monofractal process. Moreover, it is interesting to note that whereas the error bars for FBM behave approximately as $1/\sqrt{n_j}$, this is not the case for CMC-LP, where the size of the confidence intervals varies only slightly with j. This confirms that the choice of weights for weighted linear fits, as proposed in [22], is appropriate for FBM. Though not optimal for multiplicative cascades, it has been shown to perform better than non-weighted regression.

6.2. Performances of parameter estimation

We quantify the performances of the estimators $\hat{\theta} \in \{\hat{\zeta}(q), \hat{c}_p\}$ by their root mean squared error,

$$\text{mse}_{N_{MC}}^{\hat{\theta}} = \sqrt{(\widehat{\mathbb{E}}_{N_{MC}}\hat{\theta} - \theta)^2 + \widehat{\text{Var}}_{N_{MC}}\hat{\theta}}, \quad (27)$$

where $\widehat{\mathbb{E}}_{N_{MC}}$ and $\widehat{\text{Var}}_{N_{MC}}$ stand for the sample mean and variance, respectively, over N_{MC} independent realizations. Estimation performance results are summarized in Table 2 and illustrated in Fig. 6, both for wavelet coefficients and leaders, for medium size images ($N = 1024$). In addition, Table 2 shows complementary results for large images of CMC-LP ($N = 2048$). On overall, we observe that leader based estimations are more efficient than coefficient based ones.

Positive statistical moments q: For $q > 0$, both estimation procedures have approximately equal mse and std. Wavelet coefficient based estimations are slightly more efficient for monofractal FBM while leader based ones are for multifractal CMC-LP.

Negative statistical moments q: For $q \leqslant -1$, the wavelet coefficient based estimates of $\hat{\zeta}(q)$ are not meaningful as they exhibit very large mse. Therefore, a wavelet
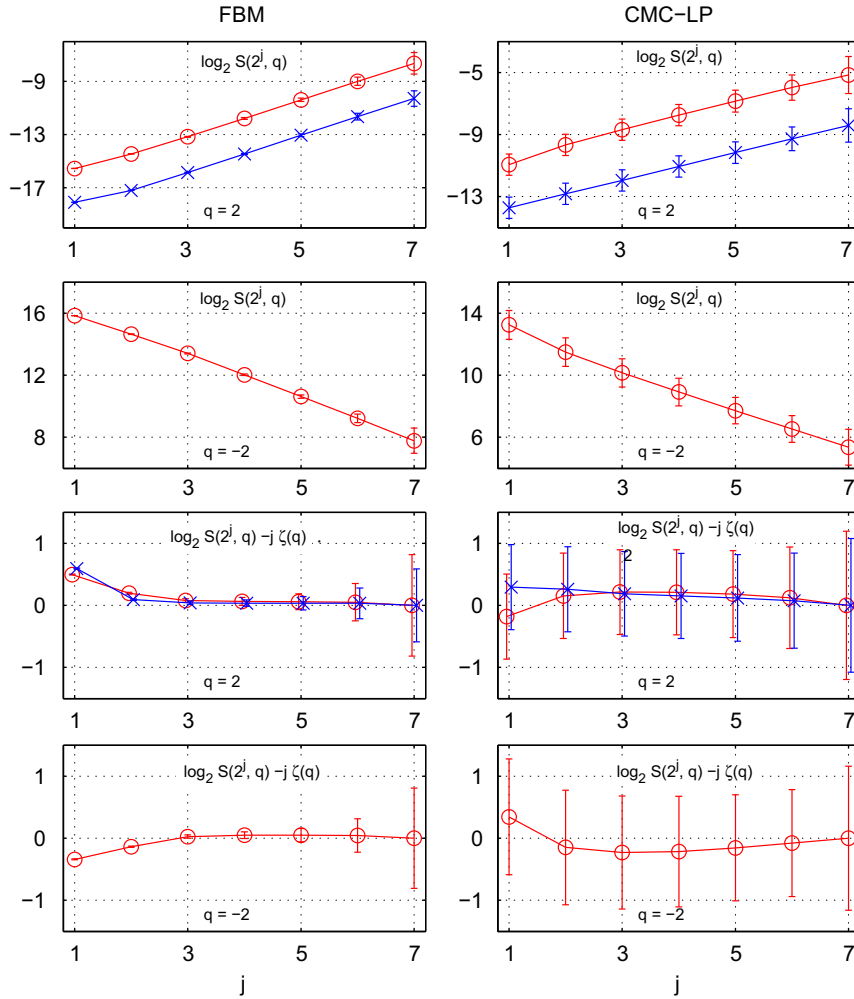
Fig. 5. *Structure functions.* Structure functions $\log_2 S(2^j, q)$ for $q = 2$ (top row) and $q = -2$ (second row), and deviation of structure functions from theoretical slope, $\log_2 S(2^j, q) - j \cdot \zeta(q)$, for $q = 2$ (third row) and $q = -2$ (bottom row), obtained by mean over Monte Carlo realizations for FBM (left) and CMC-LP (right). Red circles correspond to wavelet leader, blue crosses to wavelet coefficient based estimations. The error bars correspond to 1.96 Monte Carlo standard deviation.

coefficient based MA of images allows to explore exclusively the range $q > -1$ and thus, in practice, only the increasing part of the multifractal spectrum $\mathscr{D}(h)$. In contrast, the proposed WL based procedure permits a complete analysis of the multifractal properties of an image, and notably of the decreasing part of the multifractal spectrum (cf. Fig. 6).

Log-cumulants: Table 2 shows that the WL based estimations of c_p exhibit consistently smaller std and mse than their wavelet coefficient based counterparts. Whereas the difference in performance is only small for the estimation of c_1, it becomes more significant for c_2 and c_3, with gains in mse of up to more than one order of magnitude. This is of crucial importance, since non-zero c_2 and c_3 discriminate self-similar from multiplicative cascade processes. Further, for $N = 2048$, Table 2 (last line) enables to deduce that an asymptotic 85% confidence interval for the leader based estimation of c_3 excludes zero, hence that the real c_3 is different from zero with high

probability. To the best of our knowledge, this had never been achieved on multifractal images. It also clearly shows that for images of smaller size, the estimation of parameter c_3, a fortiori of higher order c_p, should be used with care: confidence intervals might be so large that they may not exclude 0 even if the parameters are non-zero.

Self-similar versus multiplicative cascade processes: Finally, for both the leader and coefficient based procedures, estimation is more difficult for multifractal CMC-LP than for FBM, resulting in larger mse for estimations on the multifractal process.

6.3. Bootstrap estimation performances

We evaluate the reliability of the bootstrap percentile confidence limits $\widehat{CI}_\theta$ by their recentered empirical coverage:

$$\mathscr{C}_\theta = \widehat{\mathbb{E}}_{N_{MC}} \mathbb{I}\{\theta + (\widehat{\mathbb{E}}_{N_{MC}} \hat{\theta} - \theta) \in \widehat{CI}_\theta\}, \tag{28}$$

Table 2
Estimation performance.

Estimate	theory	leaders			leaders		
		mean	std	mse	mean	std	mse
FBM − N = 1024							
$\zeta(-2)$	−1.400	−3.461	2.315	3.100	−1.388	0.022	0.025
$\zeta(-1)$	−0.700	−0.895	0.544	0.578	−0.695	0.011	0.012
$\zeta(1)$	0.700	0.699	0.010	0.010	0.696	0.012	0.013
$\zeta(2)$	1.400	1.398	0.021	0.021	1.393	0.025	0.026
c_1	0.700	0.699	0.012	0.012	0.696	0.011	0.012
c_2	0.000	0.000	0.029	0.029	0.001	0.003	0.003
c_3	0.000	0.001	0.150	0.150	−0.001	0.001	0.001
CMC-LP − N = 1024							
$\zeta(-2)$	−1.256	−3.115	2.507	3.121	−1.227	0.064	0.070
$\zeta(-1)$	−0.580	−0.718	0.546	0.563	−0.570	0.025	0.027
$\zeta(1)$	0.500	0.484	0.017	0.023	0.493	0.021	0.022
$\zeta(2)$	0.933	0.902	0.036	0.047	0.920	0.045	0.046
c_1	0.538	0.519	0.018	0.027	0.530	0.022	0.023
c_2	−0.080	−0.073	0.032	0.033	−0.077	0.015	0.015
c_3	0.014	0.005	0.152	0.152	0.011	0.013	0.013
CMC-LP − N = 2048							
c_1	0.538	0.521	0.010	0.019	0.532	0.012	0.013
c_2	−0.080	−0.073	0.016	0.018	−0.078	0.009	0.009
c_3	0.014	0.012	0.075	0.075	0.012	0.008	0.009

Mean, standard deviation and root mean squared error of wavelet coefficient (center columns) and leader (columns on the right) based estimation for FBM (top) and CMC-LP (center) for $N = 1024$, and for CMC-LP (bottom) for $N = 2048$. The columns on the left identify the parameters and their theoretical values.

where $\mathbb{I}\{\cdot\}$ is the indicator function of the event $\{\cdot\}$. The recentered coverage $\mathscr{C}_\theta$ allows to assess the performances of the confidence limits without the contribution of a potential bias in the estimation of θ. The results for $\theta \in \{\zeta(q), c_p\}$ are summarized in Table 3 for wavelet coefficient (top) and leader (bottom) based estimation and for a target coverage of 90%. We observe that for wavelet coefficient based estimation, the performances of the bootstrap confidence limits is excellent. Their actual coverage are very close to the target coverage, with error in coverage smaller than 5% both for $\zeta(q)$ and c_p, and for both processes. The performances of the WL confidence intervals is slightly inferior, with an average coverage error of approximately 9%. This can be interpreted as the result of the non-linear operation underlying the construction of leaders from wavelet, yielding an additional difficulty for bootstrap estimation. Still, the bootstrap confidence limits remain satisfactorily reliable. The use of more sophisticated and potentially more accurate double bootstrap confidence limits is currently under consideration.

6.4. Analysis of real-world image

The proposed estimation procedures have been used for the systematic analysis of large databases of real-world images (such as the texture image Univ. of Maryland data set). For illustrating its practical use, we present here the performances of the proposed estimation
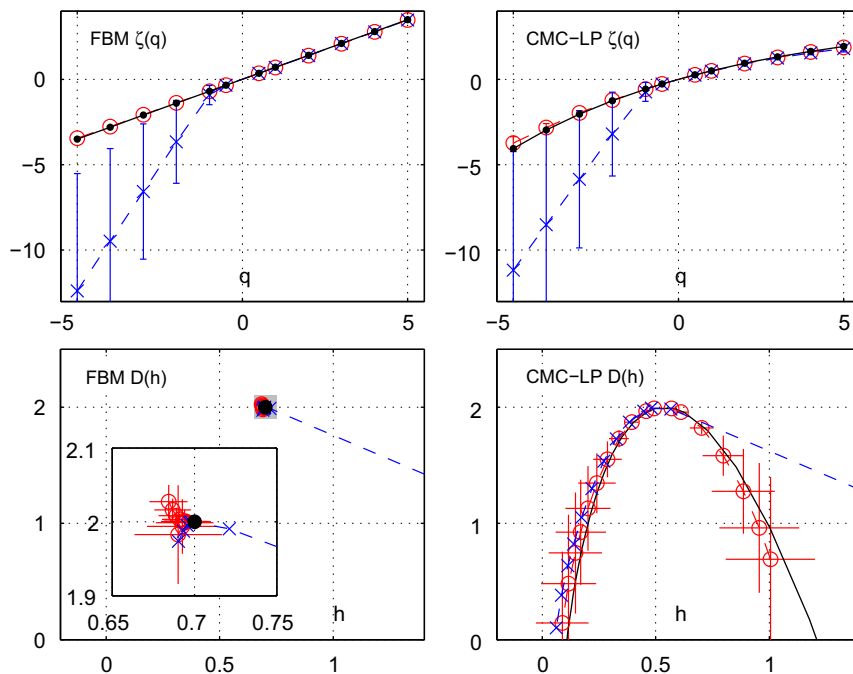
Fig. 6. *Estimates $\zeta(q)$ and $\mathscr{D}(h)$.* Estimates $\zeta(q)$ (top) and $\mathscr{D}(h)$ (bottom) for FBM (left) and CMC-LP (right), obtained from leaders (red circles, dashed lines) and wavelet coefficient (blue crosses, dashed lines) by mean over Monte Carlo realizations, and the corresponding theoretical values (black solid lines with dots). The error bars correspond to 1 Monte Carlo standard deviation. The error bars for coefficient based estimates for $\mathscr{D}(h)$ are not shown for better visibility of the spectra. The insert for $\mathscr{D}(h)$ of FBM corresponds to the area shaded around the theoretical spectra location.

Table 3
Bootstrap estimation performance.

Recentered coverage of confidence limits—target: 90%							
	$\zeta(-2)$	$\zeta(-1)$	$\zeta(1)$	$\zeta(2)$	c_1	c_2	c_3
DWT							
FBM			91.8	88.8	94.4	87.8	89.4
CMC-LP			89.0	89.2	88.2	89.8	88.2
LWT							
FBM	79.4	79.8	79.0	78.6	78.8	82.0	85.0
CMC-LP	80.8	82.0	82.6	81.2	81.0	81.2	83.0

Recentered empirical coverage (in %) of bootstrap percentile confidence limits for wavelet coefficient (top) and leader (bottom) based estimation. The empirical coverage equals the percentage of realizations for which the theoretical value of an estimate lies within the estimated confidence limits (target coverage 90%).

procedures for one real-world image of size 1024×768, taken by ourselves with a standard digital camera. It consists of trees in the Reichraminger Hintergebirge, Upper Austria (cf. Fig. 7, top). Fig. 7 shows structure functions (center), scaling exponents (bottom left) and the spectrum (bottom right) estimated from this image, obtained with the leaders based estimation procedure proposed in this work, with a $N_\psi = 3$ Daubechies' wavelet. Results on log-cumulants are summarized in Table 4. Fig. 8 illustrates the uniform regularity exponent h_{min} Eq. (18) estimate. The linear behavior of $\log_2 \sup_{m,k_1,k_2} |d_X^{(m)}(j, k_1, k_2)|$ with respect to scales j indicates the relevance of estimation of h_{min}, which is found to be clearly negative. Therefore, to handle negative minimum regularity, the image is analyzed via the (pseudo-) fractional integration procedure (cf. Section 3.3), with order $\eta = 05$ (this order is sufficient, since the estimated
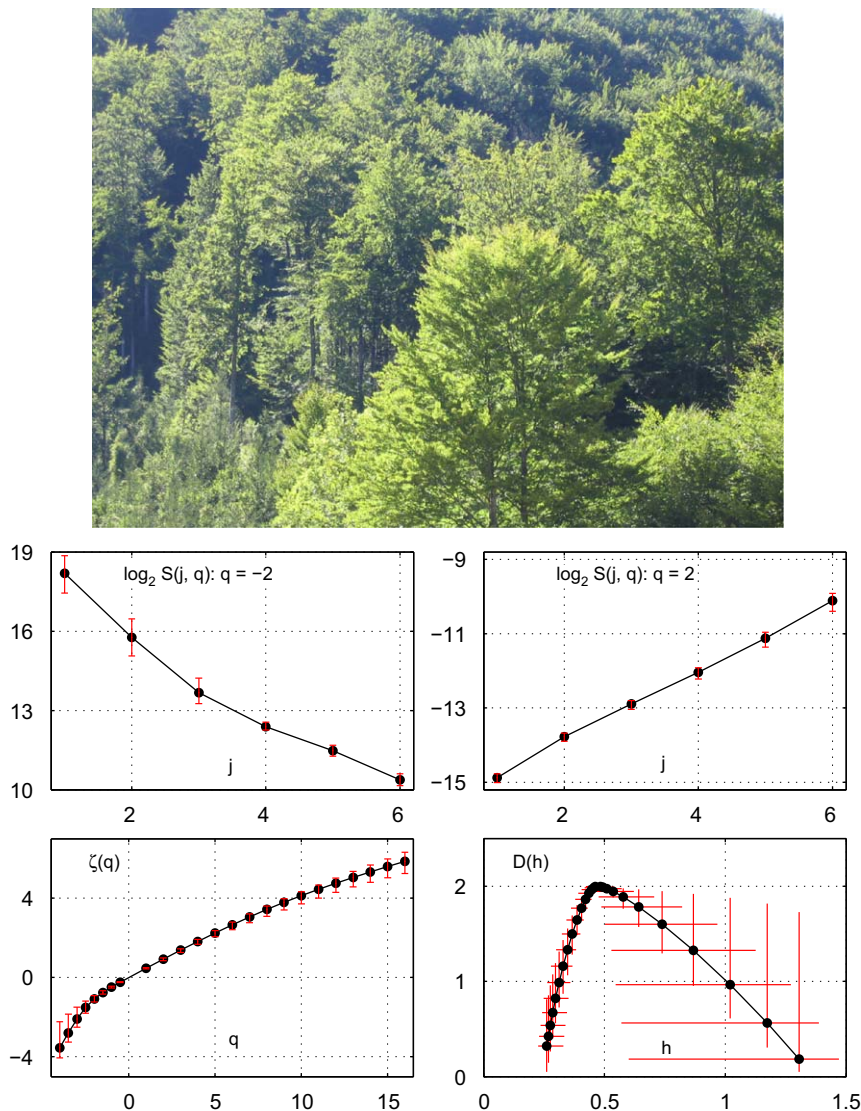

Fig. 7. *Analysis of real-world image.* Real-world image (top) and estimates: structure functions (center) for $q = -2$ (left) and $q = 2$ (right), scaling exponents $\hat{\zeta}(q)$ (bottom left) and spectrum $D(h)$ (bottom right). The bootstrap percentile 90% confidence limits are obtained from $R = 99$ resamples.

Table 4
Real-world image log-cumulants.

	$\hat{c}_1$	$\hat{c}_2$	$\hat{c}_3$
Estimate	0.472	−0.016	0.020
CI	[0.433, 0.502]	[−0.029, −0.006]	[0.005, 0.046]

Log-cumulant estimates and bootstrap percentile 90% confidence limits ($R = 99$) for the real-world image in Fig. 7 (top).
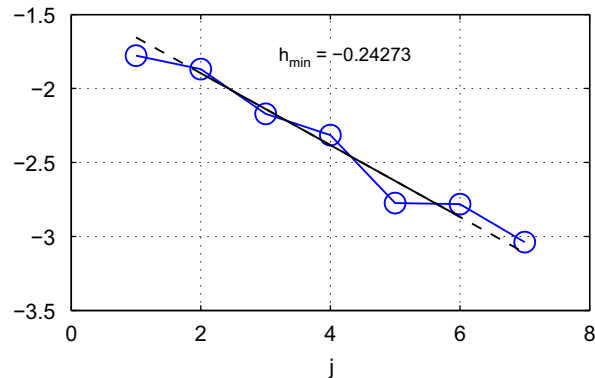
Fig. 8. *Real-world image h_{min}*. Estimate of h_{min} Eq. (18) for the real-world image in Fig. 7 (top).

uniform regularity exponent for this image is $h_{min} = -0.24$). Multifractal attribute estimates are obtained by weighted fits over the scales $2^3 \leqslant 2^j \leqslant 2^6$, for which Fig. 7 (center) indicates that $\log_2 S(2^j, q)$ are approximately linear functions of j. Results demonstrate that the proposed method can be readily applied to real-world images for their complete multifractal characterization. They demonstrate further that the bootstrap percentile 90% confidence intervals are of significant practical usefulness: first, the confidence limits on structure functions help to verify that the chosen scaling range is appropriate. Second, confidence limits on multifractal attributes allow to decide that the image shows with high probability a multifractal signature, since confidence intervals for c_2 and c_3 exclude zero. The confidence limits thus provide information that might be of significant importance for e.g., detection or classification tasks, or for the understanding of physical or biological processes underlying the data. Finally, note that the entire estimation procedure with WL MA (without bootstrap) takes less than a minute on a standard PC, whereas the same estimation with MMWT increases computation time by a factor larger than 20.

6.5. Discussion

Numerical simulations, equivalent to those reported above, have been performed on other multifractal processes and lead to similar conclusions: wavelet coefficients do not allow to meaningfully explore negative q's and thus to measure the decreasing part of the spectrum $\mathscr{D}(h)$ whereas WLs do, estimation of c_p is better when

based on leaders than on coefficients, and significantly so for $c_p, p \geqslant 2$.

Selection of scaling range: We have seen in Section 6.1 that the range of scales over which the linear fits are to be performed are likely to be narrower (requiring the use of a larger j_1) for leaders than for wavelet coefficients. For practical MA and real-world images, the choice of this regression range is a crucial, difficult and controversial issue, further complicated by the use of leaders. In practice, however, bootstrap confidence intervals for the structure functions, as obtained by the proposed procedure and illustrated in Fig. 5, constitute a precious support for solving this non-trivial issue and can be regarded as a first step towards statistical procedures for automatized or intelligently assisted detection of scales over which data are scale invariant.

Vanishing moments of wavelet: Another critical practical issue is the choice of the number of vanishing moments N_ψ for the wavelet with which the data are analyzed. Condition $N_\psi > h$, where h is the largest singularity exponent present in the data, is expected to be sufficient for a relevant MA. However, in practice, the choice of N_ψ results from a trade-off: a larger N_ψ stabilizes the estimates of the negative q structure functions and enables to get rid of potentially superimposed smooth trends such as polynomial, hence improves estimation and brings robustness; a larger N_ψ also implies a larger support for the wavelet and thus produces border effects of wider size, such that no coefficients may remain unaffected at large scales, hence in itself degrades estimation performances. Therefore, a reasonable practical rule of thumb is to choose the smallest N_ψ for which the estimated multifractal attributes do not significantly change when N_ψ is increased (i.e., remain within confidence intervals, emphasizing again the need for and the importance of such confidence intervals).

Real-world data and MA: In Section 2.2, we recalled how the estimates of $\zeta(q)$, c_p, $\mathscr{D}(q)$ and $h(q)$ are theoretically intimately tied to the multifractal spectrum $\mathscr{D}(h)$ of the field X and hence to the analysis of its local regularity fluctuations. This relation is known to hold theoretically for all the synthetic images used here for Monte Carlo simulations and illustrations. For real-world images, this interpretation in terms of multifractal spectrum and singularity description might not always be completely relevant. However, this, in no way, prevents practitioners to make use of the measured $\zeta(q)$, c_p, $\mathscr{D}(q)$ and $h(q)$ to analyze the data in terms of a less mathematically stringent formulation of scale invariance properties or to perform standard image processing tasks such as classification or retrieval based on such quantities.

Computational costs: The proposed 2D WL MA is simple both conceptually (2D DWT, leaders and linear regressions) and practically (very low computational cost, both with respect to time and memory, of the order of a 2D DWT). As an example, a 2048×2048 gray level image is processed in a couple of seconds on a standard PC under MATLAB. The bootstrap based confidence intervals are obtained essentially by repeating the linear regression procedures. The larger the repetition number and therefore the computational load, the higher the precision of

the confidence intervals. This is the unavoidable price to pay to obtain reliable confidence intervals from a single image. All the analysis and estimation procedures are designed by ourselves in MATLAB. The 2D DWT is performed using (a corrected version of) the Rice Wavelet Toolbox.

7. Conclusions and perspectives

The present contribution proposes a procedure to perform a fast, efficient and accurate analysis of the scaling and multifractal properties of images. It outperforms significantly the previous propositions based on 2D DWT or 2D CWT in estimation performances, and 2D-WTMM in computation time, memory cost and implementation complexity. It is fast and efficient since simply based on a 2D orthogonal DWT. Our procedure enables an accurate and complete characterization of the (ir)regularities of the texture of an image thanks to the use of original multiresolutions quantities called wavelet leaders, and is backed up by a strong mathematical framework.

Furthermore, the present contribution proposes and validates procedures for assessing function space model conditions for data—notably for the bounded function requirement—and handling them in practice.

The low memory and time costs together with the satisfactory estimation performance of the procedure opens for the first time the possibility to perform the MA of voluminous databases of images with possibly large sizes. Therefore, MA may be incorporated in procedures aiming at image retrieval, computer vision or robotic purposes. We are currently investigating such databases.

Moreover, for applications such as surface roughness, where one wants to understand the fracture process, or biomedicine, where one wants to detect and classify pathologies, confidence intervals are crucial. The bootstrap approach, tailored here to match image processing via the proposition of a 2D space-scale block bootstrap procedure, provides reliable and straightforwardly usable confidence intervals. This is, to the best of our knowledge, the only procedure that has been proposed to provide accurate and operational confidence intervals for MA of images. It can be further extended to devise statistical tests. This is currently investigated.

References

[1] V. Gupta, E. Waymire, A statistical analysis of mesoscale rainfall as a random cascade, J. Appl. Meteor. 32 (1993) 251–267.

[2] D. Schertzer, S. Lovejoy, F. Schmitt, Y. Ghigisinskaya, D. Marsan, Multifractal cascade dynamics and turbulence intermittency, Fractals 5 (3) (1997) 427–471.

[3] S. Roux, A. Arneodo, N. Decoster, A wavelet-based method for multifractal image analysis. III. Applications to high-resolution satellite images of cloud structure, Eur. Phys. J. B 15 (4) (2000) 765–786.

[4] R. Jennane, W. Ohley, S. Majumdar, G. Lemineur, Fractal analysis of bone X-ray computed microscopy projections, IEEE Trans. Med. Imaging 20 (5) (2001) 443–449.

[5] Y. Xu, J. Hui, C. Fermüller, Viewpoint invariant texture description using fractal analysis, Int. J. Computer Vision, 2009, to appear.

[6] F. Richard, H. Biermé, A statistical methodology for testing the anisotropy of Brownian textures with an application to full-field digital mammography, preprint.

[7] J.-L. Starck, F. Murtagh, A. Bijaoui, Image Processing and Data Analysis: The Multiscale Approach, Cambridge University Press, Cambridge, 1998.

[8] N. Decoster, S. Roux, A. Arneodo, A wavelet-based method for multifractal image analysis. II. Applications to synthetic multifractal rough surfaces, Eur. Phys. J. B 15 (4) (2000) 739–764.

[9] L. Ponson, D. Bonamy, H. Auradou, G. Mourot, S. Morel, E. Bouchaud, C. Guillot, J. Hulin, Anisotropic self-affine properties of experimental fracture surface, Int. J. Fracture 140 (1–4) (2006) 27–36.

[10] S. Peleg, J. Naor, R. Hartley, D. Avnir, Multiple resolution texture analysis and classification, IEEE Trans. Pattern Anal. 6 (4) (1984) 518–523.

[11] Y. Xu, J. Hui, C. Fermüller, A projective invariant for texture, in: Proceedings of the IEEE Conference on Computer Vision and Pattern Recognition (CVPR), New York, 2006, pp. 1932–1939.

[12] E. Bacry, J. Muzy, A. Arneodo, Singularity spectrum of fractal signals from wavelet analysis: exact results, J. Stat. Phys. 70 (3–4) (1993) 635–674.

[13] P. Abry, R. Baraniuk, P. Flandrin, R. Riedi, D. Veitch, Multiscale nature of network traffic, IEEE Signal Process. Mag. 19 (3) (2002) 28–46.

[14] S. Jaffard, B. Lashermes, P. Abry, Wavelet leaders in multifractal analysis, in: T. Qian, M.I. Vai, X. Yuesheng (Eds.), Wavelet Analysis and Applications, Birkhäuser Verlag, Basel, Switzerland, 2006, pp. 219–264.

[15] V. Sharifi-Salamantian, B. Pesquet-Popescu, J. Simoni-Lafontaine, J.P. Rigaut, A robust index for spatial heterogeneity in breast cancer, J. Microscopy 216 (2) (2004) 110–122.

[16] C.L. Benhamou, et al., Fractal analysis of radiographic trabecular bone texture and bone mineral density: two complementary parameters related to osteoporotic fractures, J. Bone Miner. Res. 16 (4) (2001) 697–704.

[17] S. Jaffard, Wavelet techniques in multifractal analysis, fractal Geometry and applications: a jubilee of Benoît Mandelbrot, in: M. Lapidus, M. van Frankenhuijsen (Eds.), Proceedings of Symposia in Pure Mathematics, vol. 72(2), AMS, Providence, RI, 2004, pp. 91–152.

[18] R. Riedi, Multifractal processes, in: P. Doukhan, G. Oppenheim, M. Taqqu (Eds.), Theory and Applications of Long Range Dependence, Birkhäuser, Basel, 2003, pp. 625–717.

[19] S. Mallat, A Wavelet Tour of Signal Processing, Academic Press, San Diego, CA, 1998.

[20] A. Arneodo, N. Decoster, P. Kestener, S. Roux, A wavelet-based method for multifractal image analysis: from theoretical concepts to experimental applications, in: P. Hawkes, B. Kazan, T. Mulvey (Eds.), Advances in Imaging and Electron Physics, vol. 126, Academic Press, New York, 2003, pp. 1–98.

[21] B. Lashermes, S. Jaffard, P. Abry, Wavelet leader based multifractal analysis, in: Proceedings of the IEEE International Conference on Acoustics, Speech, and Signal Processing (ICASSP), 2005.

[22] H. Wendt, P. Abry, S. Jaffard, Bootstrap for empirical multifractal analysis, IEEE Signal Process. Mag. 24 (4) (2007) 38–48.

[23] S. Lahiri, Resampling Methods for Dependent Data, Springer, New York, 2003.

[24] A. Zoubir, On confidence intervals for the coherence function, in: Proceedings of the IEEE International Conference on Acoustics, Speech, and Signal Processing, 2005.

[25] H. Wendt, P. Abry, Multifractality tests using bootstrapped wavelet leaders, IEEE Trans. Signal Process. 55 (10) (2007) 4811–4820.

[26] S. Jaffard, P. Abry, H. Wendt, S. Roux, B. Vedel, The contribution of wavelets in multifractal analysis, in: A. Damlamian, S. Jaffard, L.T. Tsien (Eds.), Series in Contemporary Applied Mathematics, Higher Education Press, World Scientific Publishing, 2009.

[27] J.-P. Antoine, R. Murenzi, P. Vandergheynst, S.T. Ali, Two-Dimensional Wavelets and their Relatives, Cambridge University Press, Cambridge, 2004.

[28] B. Castaing, Y. Gagne, M. Marchand, Log-similarity for turbulent flows, Physica D 68 (3–4) (1993) 387–400.

[29] J. Delour, J. Muzy, A. Arneodo, Intermittency of 1d velocity spatial profiles in turbulence: a magnitude cumulant analysis, Eur. Phys. J. B 23 (2) (2001) 243–248.

[30] H. Wendt, Contributions of wavelet leaders and bootstrap to multifractal analysis: images, estimation performance, dependence structure and vanishing moments. Confidence intervals and hypothesis tests, Ph.D. Thesis, Ecole Normale Supérieure de Lyon, France, 2008.

[31] A. Chhabra, C. Meneveau, R. Jensen, K. Sreenivasan, Direct determination of the singularity spectrum and its application to fully developed turbulence, Phys. Rev. A 40 (9) (1989) 5284–5294.

[32] M. Ossiander, E. Waymire, Statistical estimation for multiplicative cascades, Ann. Stat. 28 (6) (2000) 1533–1560.

[33] H. Wendt, P. Abry, S. Roux, S. Jaffard, B. Vedel, Analyse multifractale d'images: l'apport des coefficients dominants, Traitement du Signal, 2009, to appear.

[34] S. Jaffard, P. Abry, H. Wendt, S. Roux, B. Vedel, Wavelet analysis of multifractal measure, in preparation.

[35] Y. Meyer, Oscillating Patterns in Image Processing and Nonlinear Evolution Equations, University Lecture Series, vol. 22, American Mathematical Society, Providence, RI, 2001, the fifteenth Dean Jacqueline B. Lewis memorial lectures.

[36] P. Abry, S. Jaffard, S. Roux, B. Vedel, H. Wendt, Wavelet decomposition of measures: application to multifractal analysis of images, in: J. Byrne (Ed.), Proceedings of the NATO-ASI Conference on Unexploded Ordnance Detection and Mitigation, Springer, Berlin, 2008.

[37] S. Jaffard, Lacunary wavelet series, Ann. Appl. Probab. 10 (1) (2000) 313–329.

[38] L. Rudin, S. Osher, Nonlinear total variation based noise removal algorithms, Physica D 60 (1992) 259–268.

[39] A. Arneodo, N. Decoster, S.G. Roux, A wavelet-based method for multifractal image analysis. I. Methodology and test applications on isotropic and anisotropic random rough surfaces, Eur. Phys. J. B 15 (3) (2000) 567–600.

[40] A. Zoubir, D. Iskander, Bootstrap Techniques for Signal Processing, Cambridge University Press, Cambridge, 2004.

[41] A. Zoubir, The bootstrap and its application in signal processing, IEEE Signal Process. Mag. 15 (1) (1998) 56–76.

[42] M. Stein, Fast and exact simulation of fractional Brownian surfaces, J. Comput. Graph. Stat. 11 (3) (2002) 587–599.

[43] B. Mandelbrot, Intermittent turbulence in self-similar cascades; divergence of high moments and dimension of the carrier, J. Fluid Mech. 62 (1974) 331–358.

[44] D. Veitch, M. Taqqu, P. Abry, Meaningful MRA initialization for discrete time series, Signal Process. 80 (9) (2000) 1971–1983.